Cartesian vs radial MR-STAT: An efficiency and robustness study ☆

Oscar van der Heide [a,b,*], Alessandro Sbrizzi [a,b], Cornelis A.T. van den Berg [a,b]

[a] *Computational Imaging Group for MR Diagnostics and Therapy, Center for Image Sciences, University Medical Center Utrecht, Heidelberglaan 100, 3583 CX Utrecht, Netherlands*
[b] *Department of Radiology, Division of Imaging and Oncology, University Medical Center Utrecht, Heidelberglaan 100, 3583 CX Utrecht, Netherlands*

ABSTRACT

MR Spin TomogrAphy in Time-domain ("MR-STAT") is quantitative MR technique in which multiple quantitative parameters are estimated from a single short scan by solving a large-scale non-linear optimization problem. In this work we extended the MR-STAT framework to non-Cartesian gradient trajectories. Cartesian MR-STAT and radial MR-STAT were compared in terms of time-efficiency and robustness in simulations, gel phantom measurements and in vivo measurements.

In simulations, we observed that both Cartesian and radial MR-STAT are highly robust against undersampling. Radial MR-STAT does have a lower spatial encoding power because the outer corners of k-space are never sampled. However, especially in T2, this is compensated by a higher dynamic encoding power that comes from sampling the k-space center with each readout. In gel phantom measurements, Cartesian MR-STAT was observed to be robust against overfitting whereas radial MR-STAT suffered from high-frequency artefacts in the parameter maps at later iterations. These artefacts are hypothesized to be related to hardware imperfections and were (partially) suppressed with image filters. The time-efficiencies were higher for Cartesian MR-STAT in all vials. In-vivo, the radial reconstruction again suffered from overfitting artefacts. The robustness of Cartesian MR-STAT over the entire range of experiments may make it preferable in a clinical setting, despite radial MR-STAT resulting in a higher T1 time-efficiency in white matter.

1. Introduction

Quantitative magnetic resonance imaging ("qMRI") techniques aim to provide estimates of MR-related tissue properties like T_1 and T_2. From these tissue property maps, image contrasts can be synthesized retrospectively using signal equations for different MR sequences [1,2]. An additional advantage of qMRI over regular, qualitative MRI is that it removes scanner- and sequence induced variability in the images, which is beneficial for multi-center studies and computer aided diagnosis [3,4]. Despite its advantages, clinical adoption of qMRI is currently limited because most conventional qMRI techniques require prohibitively long scan ties and only produce one tissue parameter map at a time.

MR Fingerprinting ("MRF") is a recent multi-parametric qMRI technique which drastically reduces scan times compared to conventional qMRI methods [5]. In MRF, transient-state sequences with randomized components (e.g. flip angles, TR, TE) are used to generate "fingerprints" in each voxel. These fingerprints are measured with a highly undersampled acquisition and are subsequently matched to a pre-computed dictionary. Assuming spatio-temporal incoherence of the undersampling artefacts, the dictionary matching procedure can succesfully select the correct tissue parameters [5]. The succes of MRF approach has sparked research interest in highly accelerated, multi-parametric qMRI techniques [6,7].

In order to achieve spatio-temporal incoherence in MRF, it is beneficial to use non-Cartesian acquisition strategies [8]. In the original MRF work and most subsequent MRF studies, variably density spirals are used in the acquisition [5,9]. Radial acquisitions have also been used extensively [10–12]. Only few studies have been reported that use Cartesian (spin-warp) imaging in the context of MRF and the studies that do use such acquisitions report much longer scan times compared to the non-Cartesian MFR studies [13–15].

In a different direction from MRF, qMRI has seen advancements in the form of non-linear volumetric inversion methods that directly estimate tissue parameters from measured k-space (or "time-domain") data

---

[16]. A benefit of using a such a time-domain signal model is that the sampling of spatial frequencies that are required by the Nyquist criterion can be distributed among different contrasts [17]. That is, the *spatial encoding* and the *dynamic encoding* (i.e. T_1 and T_2 encoding) are intertwined. These techniques have initially been proposed in the context of pulse sequences for which analytical signal models are available [18–20].

Magnetic Resonance Spin Tomography in Time-domain ("MR-STAT") is a recently proposed multi-parametric qMRI framework [21] that combines the idea of non-linear, volumetric inversion together with the use of generic, transient-state sequences for performing multi-parametric qMRI. For transient-state sequences, each contrast is usually highly undersampled (typically only one readout per contrast is acquired in MR-STAT), yet by applying the non-linear volumetric inversion it is still possible to reconstruct high-quality quantitative parameters maps from the data [22]. The MR-STAT reconstruction procedure relies on a forward model that relates multiple quantitative tissue parameters maps directly to the measured time-domain (k-space) signal. Evaluation of the forward model involves numerical integration of the Bloch equations as, in general, no analytic signal models are available for the type of time-varying flip angle sequences used in MR-STAT. The forward model gives rise to a large-scale non-linear inversion problem which is solved through iterative algorithms that require computing partial derivatives of the forward model with respect to all tissue parameters. In addition, instead of using the (non-uniform) Fast Fourier Transform ("FFT") for transforming back and forth between image space and spatial frequency space, the gradient encoding is taken into account explictly within the Bloch simulations. In other words, the spatial and dynamic encoding are simultaneously modeled. The MR-STAT reconstruction is computationally challenging and requires dedicated algorithms to manage computation times as well as computer memory requirements [22–24].

The feasibility of the MR-STAT approach has been demonstrated in previous work with acquisitions that rely on Cartesian gradient trajectories. High-resolution (1 mm in-plane) 2D quantitative T_1, T_2 and proton density maps were reconstructed from in vivo brain data acquired in scan times comparable to what is reported in MRF studies using non-Cartesian acquisitions [22,24]. The theory behind the MR-STAT concept, however, is not restricted to Cartesian acquisitions. To demonstrate the generic nature of MR-STAT, in the current work we have extended the framework to non-Cartesian acquisitions. This allows us to compare Cartesian and non-Cartesian trajectories within MR-STAT.

The main aim of this paper will be to perform an empirical comparison of Cartesian and radial MR-STAT reconstructions performed on both simulated and measured data. The focus will lie on the efficiency and robustness of the two different encoding strategies. Efficiency is interpreted in this context as $T_{1,2}$-*to-noise* ratio per square root of scan time [25]. The efficiency is assumed to capture both the spatial and dynamic encoding capabilities of an acquisition. Robustness of the iterative reconstruction procedures against model inaccuracies (e.g. hardware imperfections) and reconstruction parameters (e.g. the number of iterations used) will also be studied since they can have a significant impact on efficiency as well.

For conventional, qualitative MR imaging, it is known that, for example, radial trajectories have a lower SNR efficiency due to the non-uniform sampling density [26]. That is, in terms of *spatial* encoding, radial is less efficient than Cartesian. However, we expect non-Cartesian MR-STAT acquisitions to potentially have higher *dynamic* encoding capabilities based on the following reasoning. The transient-state nature of the MR-STAT acquisition implies that the underlying image contrast is constantly changing. Image contrast information is mostly contained in the central region of k-space. With non-Cartesian acquisitions like radial and spiral, the center of k-space can be sampled with each readout and thus each readout can provide information about the changing contrast. On the other hand, with a Cartesian acquisition, readouts that sample

the outer parts of k-space are expected to provide relatively little information on the underlying contrast changes and thus provide less dynamic encoding power compared to the central k-space lines. Because in MR-STAT both spatial and dynamic encoding is required, it is a priori unclear which trajectory type will result in a higher efficiency.

The choice to consider radial acquisitions in this work - as opposed to other non-Cartesian trajectories - is motivated by the fact that most acquisition parameters like TR, TE, total number of readouts, number of samples per readout, readout bandwidth and total scan time can be kept similar for both. With, for example, spiral trajectories, one typically acquires fewer readouts with longer TRs and more samples are acquired per readout depending on the design of the spirals. A comparison of Cartesian against other non-Cartesian acquisitions thus requires many design choices that may influence the outcomes.

To study the efficiency and robustness question in the context of Cartesian and radial MR-STAT, we proceed as follows. Assuming that a pulse sequence is used that has sufficient T_1 and T_2 encoding power, and assuming that the MR-STAT reconstructions have succesfully converged, errors in the final parameters maps are caused by either 1) thermal noise on the data, 2) undersampling artefacts and/or 3) inaccuracies in the forward model (e.g. hardware imperfections, partial volume effects or unmodelled biophysical phenomena). Since the model-based MR-STAT reconstruction is expected to be highly robust against undersampling, we expect errors from undersampling to be minimal for both the Cartesian and radial cases. To verify whether this is the case, we will first perform numerical simulations without thermal noise or model imperfections such that undersampling artefacts are the only expected error source. Afterwards, we will study the efficiency and robustness in the presence of thermal noise by adding (complex) Gaussian noise to the simulated data. We then proceed by performing gel phantom and in vivo measurements where also model imperfections are expected to be present.

2. Methods

2.1. MR-STAT

In MR-STAT, the forward model for the measurable time-domain signal s after spatial discretization is given by

$$s(t) = \sum_{j=1}^{N_v} m(\boldsymbol{\theta}_j, t) e^{-2\pi i k(t) \cdot r_j} \Delta_V. \qquad (1)$$

Here N_v is the number of voxels within the field-of-view, Δ_V is the volume element for each voxel, r_j is the vector of spatial coordinates for the voxel associated with index j, $\boldsymbol{\theta}_j$ is the vector of MR-relevant biophysical tissue properties (e.g. $T_1, T_2, \rho, \ldots$) for the voxel associated with index j, $k(t)$ is the k-space trajectory and m is the complex transverse magnetization whose time-varying behavior is modeled by the Bloch equations. For simplicity, we do not include receive coils in the forward model in here but it should be noted that within the actual MR-STAT reconstructions data from multiple coils is taken into account [22]. Let $t_1, \ldots, t_{N_t}$ denote the sampling times with N_t the total number of samples and define the vector of time-domain samples s

$$s := [s(t_1), \ldots, s(t_{N_t})] \in \mathbb{C}_\mathfrak{t}^\mathbb{N}.$$

Note that s depends on the tissue parameters $\boldsymbol{\theta}_j$ for all voxels j. All tissue parameters are concatenated into a single vector $\boldsymbol{\alpha}$. The forward model (Eq. (1)) then gives rise to a large-scale non-linear inverse problem

$$\boldsymbol{\alpha}^* = \operatorname{argmin}_\alpha \frac{1}{2} \|\boldsymbol{d} - \boldsymbol{s}(\boldsymbol{\alpha})\|_2^2. \qquad (2)$$

This inverse problem is numerically solved using a Gauss–Newton method that requires the computation of partial derivatives of the objective function at each iteration [22].

Instead of using the (non-uniform) FFT to evaluate an approximation to the forward model (Eq. (1)) as is common in other frameworks (e.g. MRF), in MR-STAT the forward model (Eq. (1)) is evaluated directly. Both Cartesian and non-Cartesian gradient trajectories $k(t)$ can be inserted into the forward model. In the case of non-Cartesian trajectories, no gridding or density compensation are required as opposed to typical non-uniform FFT implementations. Also note that, in principle, spin dynamics during readouts (e.g. $T_2^{(*)}$−decay or off-resonance induced rotations) can be modeled. These effects are expected to be neglible for acquisitions with short readouts and therefore exploring potential benefits of including these dynamics in the forward model is outside the scope of the current work.
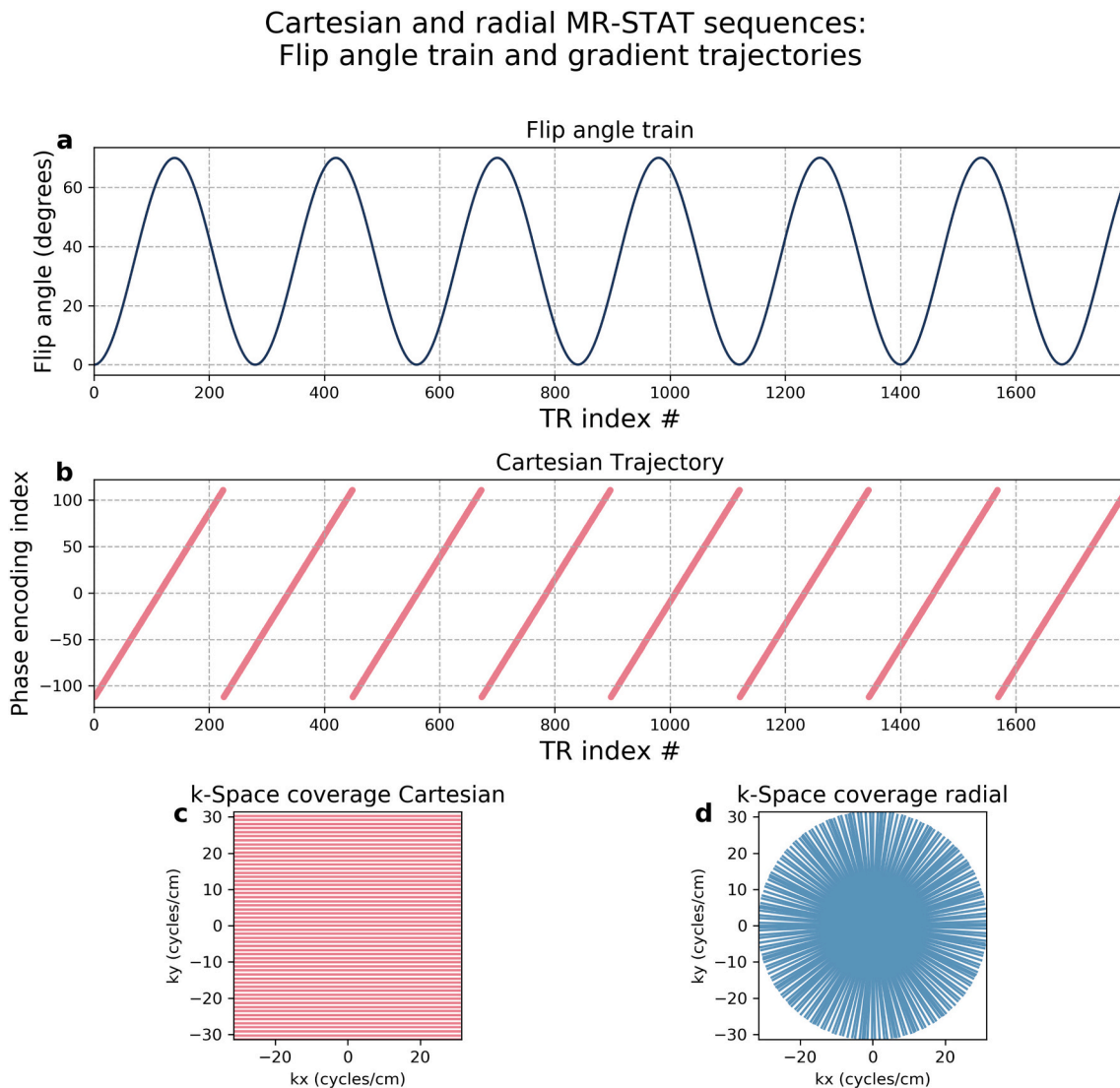
2.2. Acquisition

2.2.1. Numerical brain phantom simulations

To compare the theoretical efficiency of both Cartesian and radial acquisitions in the context of MR-STAT, we first perform a simulation study for which ground truth parameter values are available. A 2D numerical brain phantom [27] was generated consisting of several compartments with different combinations of T_1, T_2 and proton density values. The field-of-view of the phantom was set to 224 mm x 224 mm with an in-plane resolution of 1 mm x 1 mm, resulting in a matrix of 224×224 voxels. In a conventional (qualitative) MR setting, a minimum of 224 phase encoding lines would need to be acquired for the Cartesian case to satisfy the Nyquist criterion. In a radial setting, a minimum number of $\pi/2 \times 224$ would need to be acquired [28] to satisfy the Nyquist criterion.

For the MR-STAT acquisitions, a gradient-spoiled sequence consisting of 1792 ($= 8 \times 224$) TR's was employed with a varying flip angle train such that the flip angle at the n-th TR was given by $35 \times 1 - \cos(2n/280)$ (resulting in a sinusoidal pattern of flip angles between 0 and 70 degrees, see Fig. 1a). For the Cartesian case, linear ordering of the 224 different phase encoding lines was chosen and the pattern is repeated eight times (Fig. 1b middle row). For the radial trajectory the first readout was identical to the Cartesian $k_y = 0$ line, and subsequent readout lines were obtained by rotating the previous readout line with the golden angle, resulting in 1792 different radial angles with a very dense cumulative sampling of k-space. The TR and TE remained fixed throughout the sequence with values of 8.8 ms and 4 ms, respectively. For each of the 1792 readouts a total number of 448 samples per readout (corresponding to a readout oversampling factor of two) were simulated. The total simulated acquisition time was 15.8 for both the Cartesian and the radial case. s. The k-space coverage for both

Cartesian and radial MR-STAT sequences:
Flip angle train and gradient trajectories

Fig. 1. [**a**] Flip angle train used for both the Cartesian and radial acquisitions. [**b**] The phase encoding order for the Cartesian acquisitions. [**c** and **d**] K-space coverage for the Cartesian and radial acquisitions, respectively. Note that the Cartesian sampling scheme is repeated eight times.

acquisitions is depicted in Fig. 1c and d, respectively.

The magnetization response in each voxel was simulated using the Extended Phase Graph ("EPG") method [29]. In these simulations, a Gaussian-shaped RF excitation waveform was used and the corresponding slice profile was modelled by partitioning each voxel into 35 compartments that experience different effective flip angles (i.e. the partitioned EPG method [23,26]). The scaling factors to determine the effective flip angles were obtained from simulating the magnetization response at different z-locations for all the different RF-excitation waveforms corresponding to different flip angles. Using the MR-STAT forward model (Eq. (1)), time-domain data was simulated for both Cartesian and radial readout trajectories. The simulation code was written in the Julia programming language [4] and the simulations were performed on an NVIDIA GeForce RTX A5000 graphics card.

To study the efficiency and robustness in the presence of thermal noise, we corrupted the noiseless datasets with random noise sampled from a complex Gaussian distribution. The noise was generated such that the signal-to-noise ratio in decibels (SNR_{DB}) was 15.36 DB for the Cartesian case. The SNR_{DB} is computed as

$$SNR_{DB} = 10\log_{10}\left(\frac{RMS(\text{signal})^2}{RMS(\text{noise})^2}\right),$$

where $RMS(x)$ is the root mean square of a vector x. The same noise vector was added to the radial dataset.

2.2.2. Gel phantom measurements

Twelve vials containing gadolinium-doped gel with varying T_1 and T_2 values (TO5, Eurospin II test system, Scotland) were scanned using a 3T Philips Ingenia Elition X MR System (DDAS spectrometer, software release 5.6) with the vendors 16-channel receive headcoil. Data from a single 2D slice was acquired using Cartesian and radial sequences similar to the ones used the simulation study. In both cases the in-plane resolution was 1 mm x 1 mm, the field-of-view was 224 mm x 224 mm and slice thickness was 5 mm. A total number of 1792 readouts were acquired with 448 samples per readout (factor two readout oversampling) with a readout bandwith of 85.6 kHz. For both acquisitions, the TE and TR were set to their shortest possible values. For the Cartesian acquisition the TE was 3.8 ms and the TR was 7.5 ms, resulting in a scan time of 13.4 s. For the radial acquisition, the TE and TR were slightly different at 4 ms and 8.5 ms, respectively, resulting in a total scan time of 15.2 s.

In addition to the MR-STAT scans, inversion-recovery single spin-echo T_1 measurements as well as single echo spin-echo T_2 measurements were performed to obtain reference parameter values for the vials. For the T_1 mapping measurement, inversion times of $[50, 100, 150, 350, 550, 850, 1250]$ ms were chosen and for the T_2 mapping measurement echo times of $[8, 28, 48, 88, 138, 188]$ ms were chosen. The T_1 and T_2 values were obtained pixel-wise by fitting (non-linear) exponential regrowth (T_1) and exponential decay (T_2) curves to the measurements using the variable projection method [30].

2.2.3. In-vivo measurements

In-vivo measurements were performed on a healthy volunteer after having obtained written informed consent. The same scanner hardware acquisition settings were used as for the gel phantom measurements, except that for the Cartesian acquisition the TR, TE and total scan time were 7.7 ms, 4.0 ms and 13.8 s, respectively. For the radial acquisition the TR, TE and total scan time were 8.6 ms, 4.0 ms and 15.4 s, respectively.

2.3. MR-STAT reconstructions

To reconstruct quantitative parameter maps from the data, the matrix-free Gauss–Newton MR-STAT method proposed in van der Heide et al. [22] was used to reconstruct quantitative parameter maps from the

data. Within this method, the magnetization response in each voxel was simulated using the EPG method with the same slice profile correction technique and computer hardware as described in Section 2.2.1. Partial derivatives of the magnetization response were computed using finite differences. The initial parameter estimates for T_1 and T_2 were set to 1.0 s and 0.1 s, respectively. The proton density was initialized by inserting the initial T_1 and T_2 values into Eq. (2), which then reduces to a linear problem that can be solved using the LSQR algorithm [31]. Given the initial proton density, a spatial mask was generated by selecting the voxels for which the magnitude of the initial proton density was higher than 10 % of the maximum magnitude. The maximum number of outer iterations of the iterative reconstruction algorithm was set to twenty and the number of Conjugate Gradient iterations within each outer iteration was set to twenty as well.

Raw data from the scanner was exported using ReconFrame (Gyrotools, Switzerland). In all reconstructions on measured data, the singular value decomposition was applied prior to the reconstruction to generate virtual coil data [32]. The number of virtual coils was chosen such that approximately 85% of the total energy was captured (i.e. the sum of the singular values was approximately 0.85). Coil sensitivity maps were estimated from the measured data using the ESPIRiT algorithm [33]. To correct for B_1^+ inhomogeneities that may be present at 3T, we measured a B_1^+ map separately using the dual angle method [34]. This B_1^+ map was then used in the reconstruction model to scale the effective RF induced flip angles in each voxel.

For the radial acquisitions, the outer corners of k-space are never sampled, as can be seen from Fig. 1d. In conventional non-uniform FFT based MR reconstructions, this is not necessarily problematic since the gridding procedure essentially zero-fills these non-sampled k-space regions. However, for iterative reconstruction techniques like MR-STAT, these non-sampled regions can cause strong noise amplification [35]. We therefore filter the reconstructed quantitative parameter maps by applying a circular symmetric window function in the Fourier domain as after the MR-STAT reconstruction. For the gel phantom data, the arctan-based filter proposed by Pruessmann et al. [35] was used with a cutoff of value set to $k_{x,max}$ and $\beta = 100$. For the in vivo data, we used the Hann filter defined as

$$k \to \cos\left(\frac{\sqrt{k_x^2 + k_y^2}}{|k_{max}|}\right)^2$$

where k is the k-space coordinate. The same filters will be applied to parameter maps obtained from Cartesian and radial data, respectively.

2.4. Efficiency assessment

The time-efficiency of the acquisitions will be computed as

$$\frac{T_n NR}{\sqrt{T_{scan}}}, \quad n = 1, 2,$$

where $T_n NR$ is the T_n-to-noise ratio and T is the scan time [25]. For the numerical brain phantom, we compute the $T_n NR$ ($n = 1, 2$) for each tissue type separately by dividing the mean T_n value by the standard deviation of the T_n value for that tissue type. For the gel phantom measurements, values for $T_n NR$ are obtained in a similar fashion by computing the mean values and standard deviations in manually drawn regions-of-interest in each vial. For the in vivo measurements, gray- and white matter segmentation is performed using the T_1 maps as input to FSL Fast [36] and the $T_n NR$ values are computed in these regions.

Because the MR-STAT reconstructions follow an iterative procedure, one question that needs to be addressed is which iterations will be used for analyzing the efficiency. For this purpose, whenever ground truth parameter maps are available, the root mean squared relative errors ("RMSRE") is utilized. If α^{gt} denotes the vector of ground truth

parameter values, the RMRSE value for the current estimates of the tissue parameter α is computed as

$$RMRSE(\boldsymbol{\alpha}) \left(\frac{1}{N_p} \sum_{j=1}^{N_p} \left(\frac{\alpha_j - \alpha_j^{gt}}{\alpha_j} \right) \right)$$

The iterations with minimum RMSRE value are assumed to strike a balance between bias and precision. To assess the robustness of the reconstructions against overfitting, the efficiencies will also be computed at the final iterations in each case. Note that in the in vivo case, no ground truth parameter values are available so the RMSRE cannot be computed and therefore only the final iterations are considered.

3. Results

3.1. Numerical brain phantom simulations

3.1.1. Noiseless dataset

In Fig. 2 the T_1 and T_2 maps reconstructed from the noiseless numerical brainweb phantom datasets are displayed, as well as the relative error maps. The RMRSE values for each iteration are shown in Fig. 3. In the Cartesian case, the relative errors and RMSRE value at iteration twenty are neglibly small. The parameter maps are reconstructed without apparent aliasing artefacts despite each contrast (i.e. each TR) being sampled with only one Cartesian readout line. The Cartesian acquisition thus has sufficient spatial and dynamic encoding power.

In the radial case we do observe non-neglible errors in the parameter maps and the RMSRE value is orders of magnitude higher compared to the Cartesian case. We argue that the higher errors are not resolved by acquiring more spokes per contrast or running more iterations in the
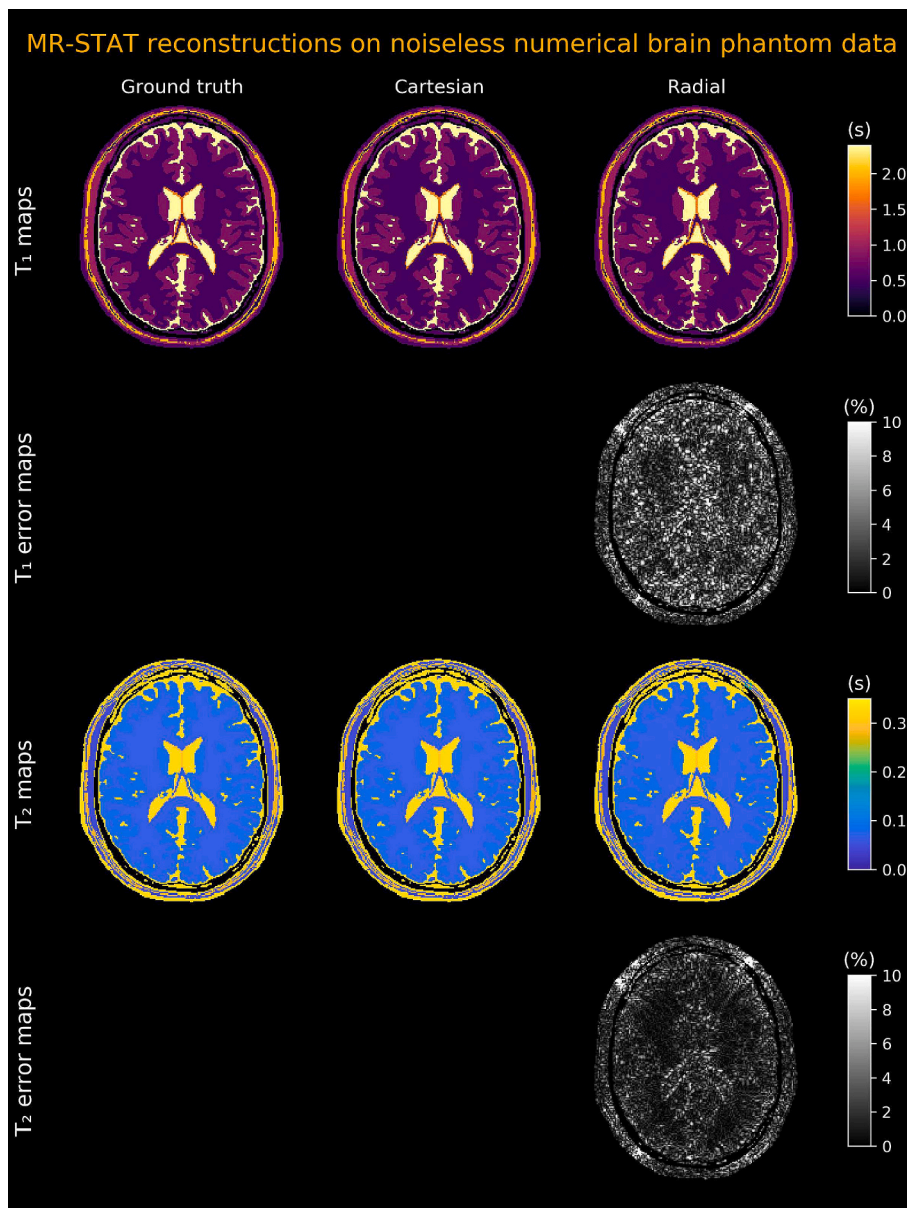

Fig. 2. The T_1 and T_2 parameter maps reconstructed from noiseless simulated brain data. The first column shows the ground truth T_1 and T_2 maps. The second column shows the parameter maps and relative error maps for the Cartesian case after twenty iterations. The third columns shows the parameter maps and relative error maps at iteration twenty for the radial case.

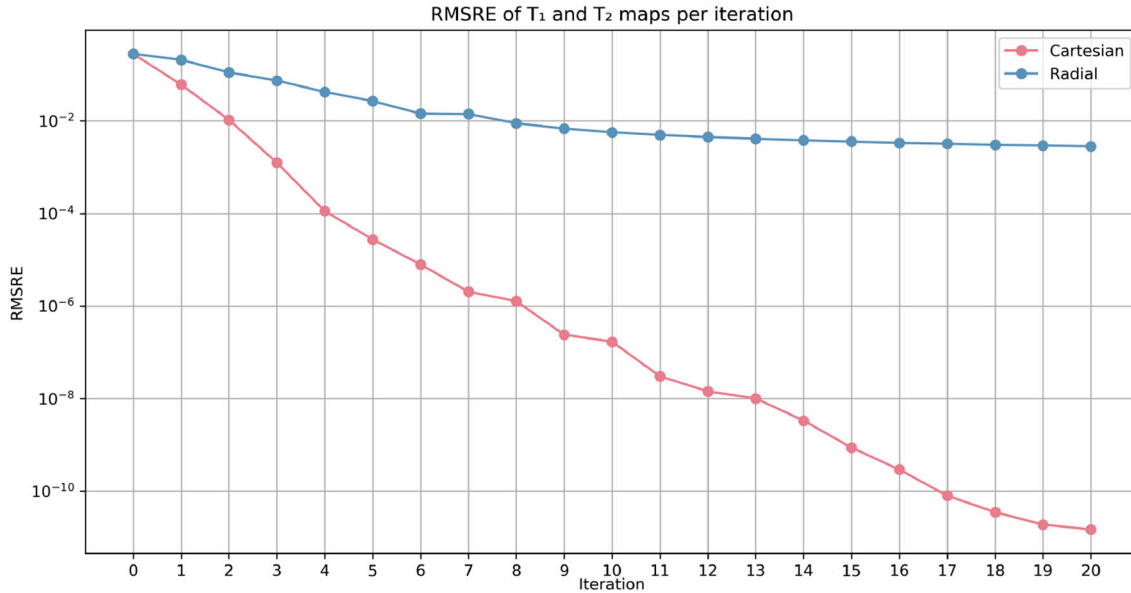## Convergence of MR-STAT reconstructions on noiseless numerical brain phantom data

Fig. 3. RMRSE values (for T_1 and T_2 combined) per outer iteration. For the radial case the RMRSE values are higher because the outer corners of k-space are never sampled and therefore finer structures in the parameter maps cannot be properly resolved (i.e. reduced spatial encoding).

reconstruction procedure. Instead, this reduced *spatial* encoding power of the radial acquisition is the result of not sampling the outer corners of k-space (see Fig. 1d). This makes it impossible for the reconstruction procedure to properly resolve the finer structures in the parameter maps.

In Supplementary Material S1 we adjusted the radial k-space trajectory to also sample the outer corners to improve the spatial encoding. In that situation we indeed observe that the parameter maps are properly reconstructed with neglibly low relative errors and RMSRE values. The errors - although neglible - are still higher compared to the Cartesian case, but this is expected because, unlike in the Cartesian case, the image grid does not exactly match with the sampling grid.

3.1.2. Noisy dataset
In Fig. 4a the cost $\left(\left(\boldsymbol{\alpha} \mapsto \frac{1}{2}\|\boldsymbol{d} - s(\boldsymbol{\alpha})\|_2^2\right)\right)$ is plotted for each iteration of

the MR-STAT reconstructions on the noisy numerical brain phantom datasets. Since the model used to simulate the data is equal to the model used in the reconstruction, upon convergence, the cost function is expected to be similar to $\frac{1}{2}\|\boldsymbol{\eta}\|_2^2$, where $\boldsymbol{\eta}$ denotes the vector of complex noise that was added to both datasets. The noise level $\frac{1}{2}\|\boldsymbol{\eta}\|_2^2$ is plotted as a horizontal line and it can be seen that for both reconstructions, the noise level is indeed reached. In Fig. 4b the RMRSE values per iteration of the MR-STAT reconstruction algorithm are shown. No filtering was applied to these reconstructions. Iterations three and eight results in the lowest RMSRE values for the Cartesian and radial cases, respectively. At these *optimal* iterations, the RMSRE value for radial is lower than for Cartesian. After the optimal iterations, the RMSRE values go up slightly whereas the cost functions decrease, suggesting that the reconstructions may be susceptible to overfitting artefacts.

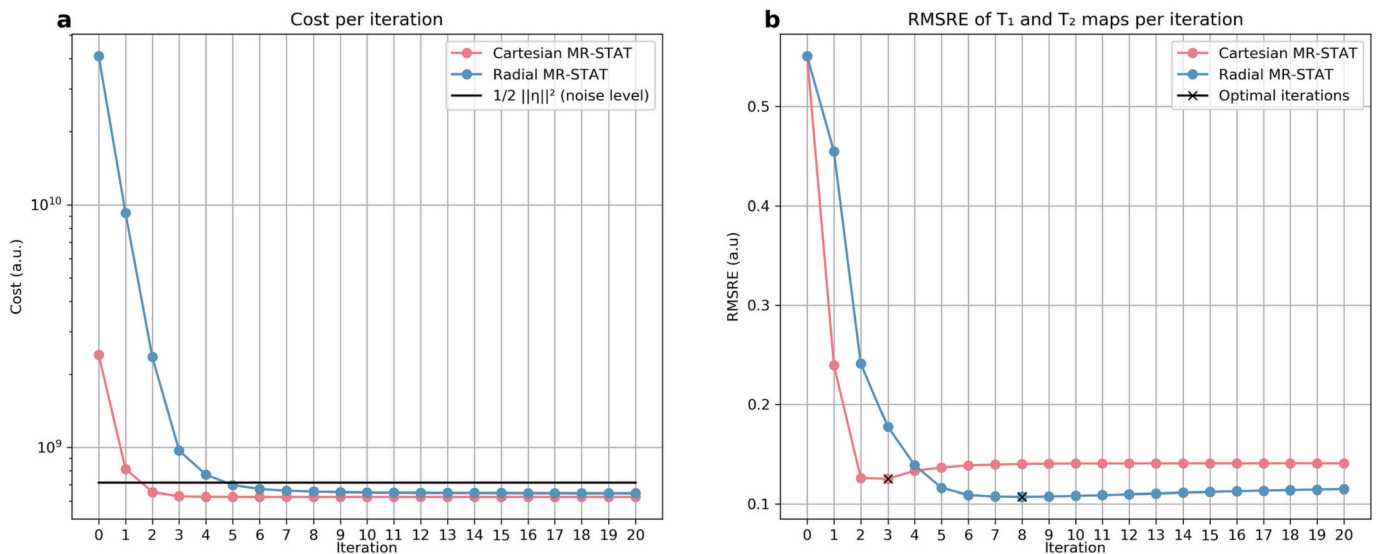## Convergence of MR-STAT reconstructions on noisy numerical brain phantom data

Fig. 4. Reconstruction results for the noisy numerical brain phantom dataset. **a**: Cost as function of the number of outer iterations. **b**: RMRSE values (for T_1 and T_2 combined) per outer iteration.

The reconstructed parameter maps and relative error maps at the optimal iterations are shown in Fig. 5 together with the parameter maps at the final iterations. Like in the noiseless case, no apparent undersampling artefacts are observed. Although the increase of the RMSRE value suggests that the reconstructions may be susceptible to overfitting, it is visually difficult to observe for both the Cartesian and the radial case. That is, the reconstructions appear to be robust against simulated thermal noise.

The mean T_1 and T_2 values as well as standard deviations per compartment at the optimal iterations as well as the final iterations are shown in Fig. 6a-b. It can be observed that the mean tissue parameter values per compartment are in good agreement with the ground truth values (well within one standard deviation). The efficiencies per compartment are displayed in Fig. 6c-d. We see that at the final iterations, the radial acquisition results in higher efficiencies (approximately 25%) for T_2 in six out of the seven distinct tissues despite the radial reconstruction suffering from errors caused by not sampling the outer corners of k-space. For T_1, the Cartesian acquisition is more efficient for four out of the seven tissues, but in gray- and white matter (arguably the most relevent tissues for most brain imaging applications) the radial acquisition is more efficient.

3.2. Gel phantom measurements

To assess the efficiency and robustness of the MR-STAT reconstructions on the Cartesian and radial data obtained from gel phantoms, we follow a similar procedure as in the numerical brain phantom study. In Fig. 7a the RMRSE values for each iteration are shown. The RMSRE values for the Cartesian case follow a similar curve as in the noisy numerical brain phantom case and iteration two is observed to result in the lowest RMSRE value. For the radial case, the situation is different compared to the noisy numerical brain phantom case. Without filtering the parameter maps in a post-processing step, the lowest RMSRE occurs at iteration three but at further iterations the RMSRE values rapidly increases, indicating that the radial case is highly susceptible to overfitting.

In Fig. 8 the T_1 and T_2 parameter maps for the MR-STAT reconstructions of the gel phantom data are shown. In columns one and two the maps from the Cartesian acquisition are shown at iterations two and twenty, respectively. Some mild overfitting artefacts (e.g. high frequency noise) can be observed in the maps corresponding to iteration twenty when compared to iteration two. On the other hand, when comparing iterations three and twenty for the radial acquisition (columns four and five, respectively), the appearance of strong overfitting artefacts can indeed be observed. Therefore, the application of a window function to the parameter maps in Fourier domain is deemed necessary. In this case, an arctan-based filter was chosen [35]. The resulting RMSRE curves are displayed in Fig. 7b and in Fig. 8, columns three and six, the filtered parameter maps are displayed as well. We observe that the RMSRE values for the radial case stabilize to values comparable to the
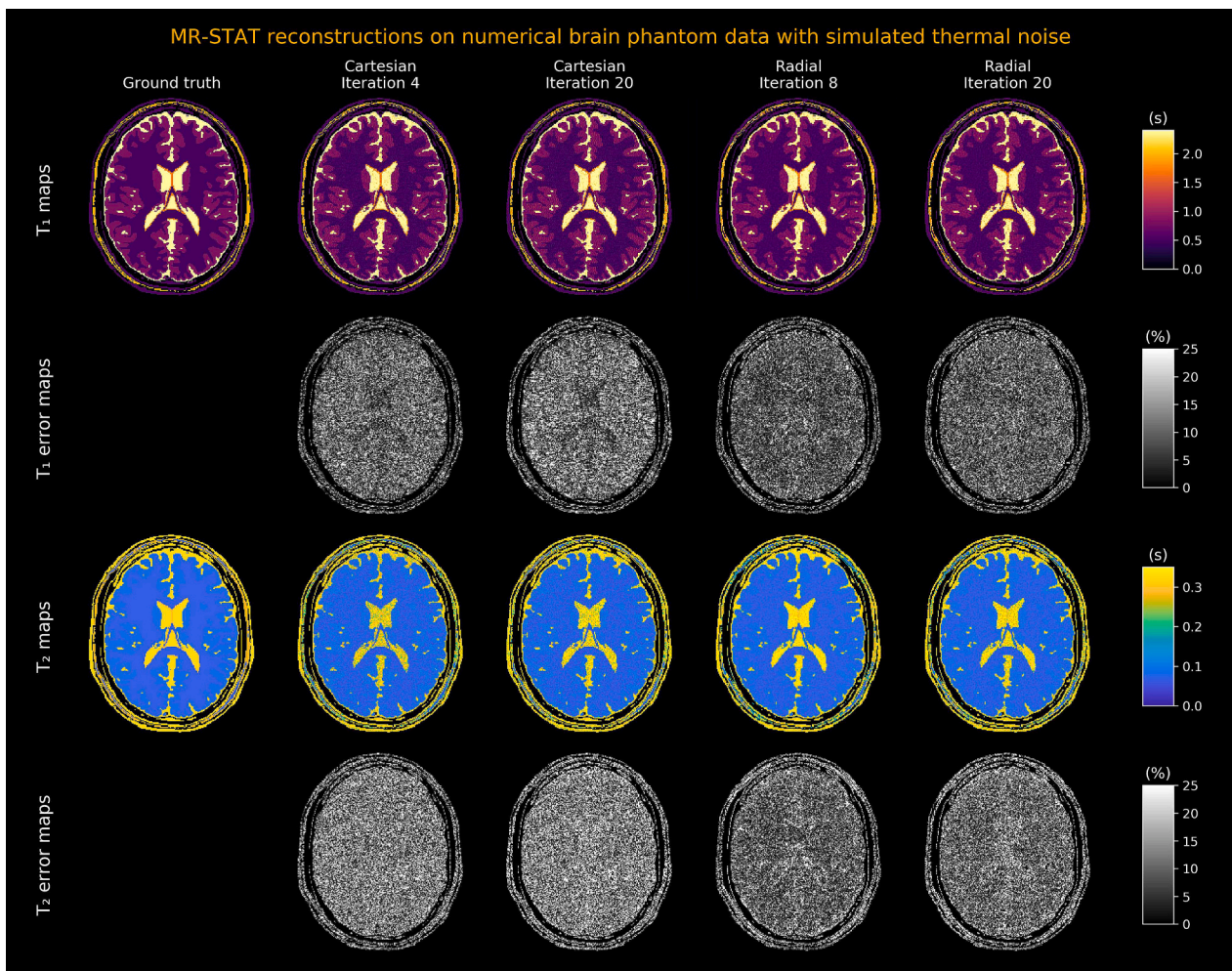

Fig. 5. The T_1 and T_2 parameter maps reconstructed from noisy simulated brain data. The first column shows the ground truth T_1 and T_2 maps. The second and third columns show the parameter maps and relative error maps for the Cartesian case for the iteration with the lowest RMSRE value (iteration three) and the final iteration (iteration twenty), respectively. The fourth and fifth columns show the parameter maps and relative error maps for the radial case.

Efficiency assessment of MR-STAT reconstructions on numerical brain phantom data
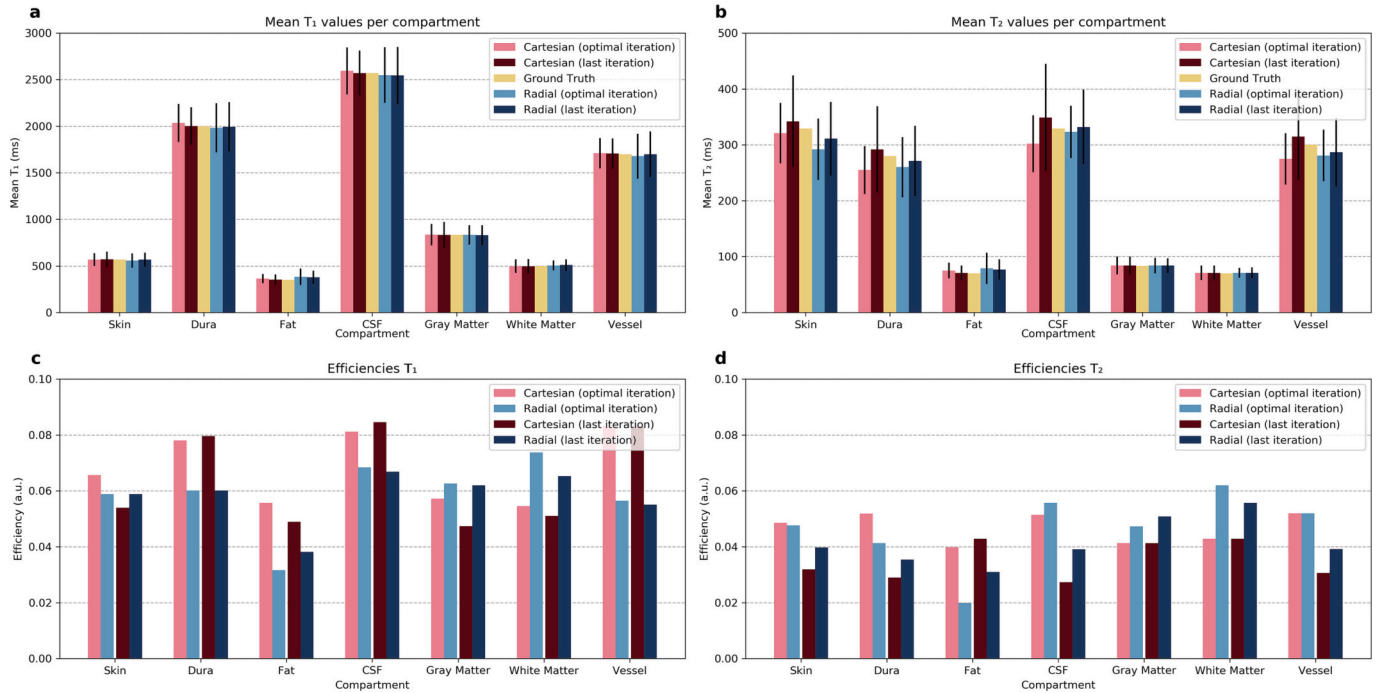
Fig. 6. **a-b**: Mean T_1 and T_2 values and standard deviations per tissue type of the numerical brain phantom reconstructions. Ground truth parameter values are displayed using the yellow bars. **c-d**: Efficiencies for T_1 and T_2 per tissue type. It can be observed that overall the radial case results in higher efficiencies.

**Convergence of MR-STAT reconstructions on measured gel tube data**
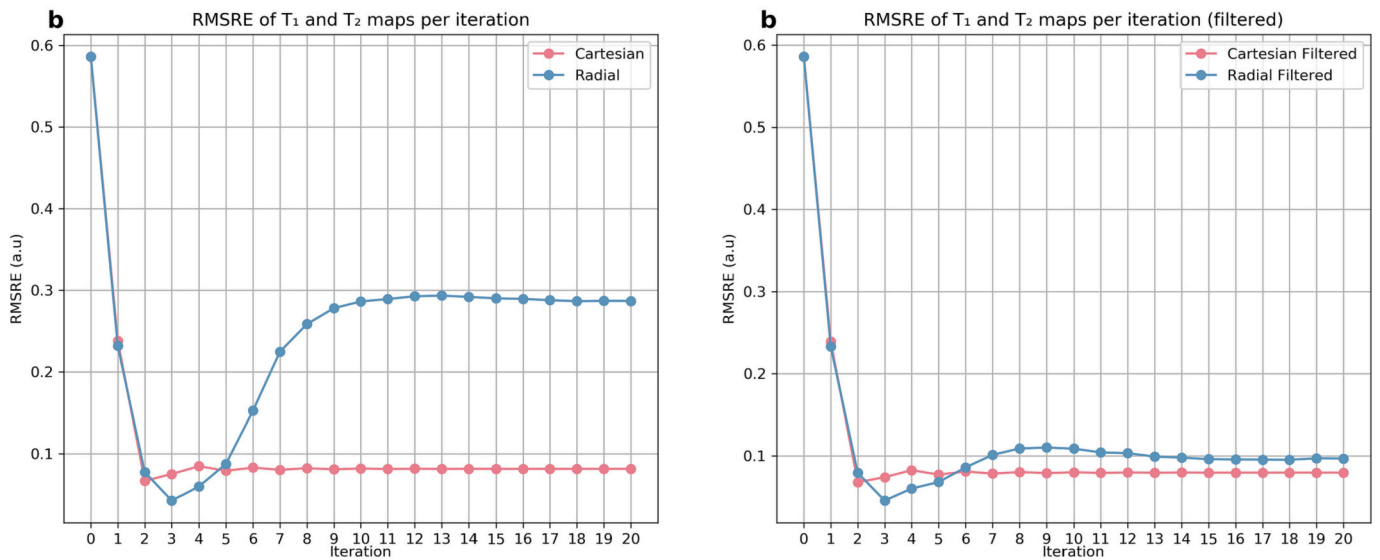
Fig. 7. Reconstruction results for the gel phantom measurements. **a**: RMRSE values (for T_1 and T_2 combined) per outer iteration. **b**: RMRSE values after applying an arctan-based filter to the parameter maps in a post-processing step.

RMSRE values and the high frequency noise in the parameter maps is greatly reduced. For the Cartesian case, this particular choice of filter has no significant impact on the RMSRE values or the parameter maps. We also visually observe that for both the Cartesian and radial cases, at the optimal iterations, the T_2 of the vial with the highest T_2 value has not fully converged yet.

The mean T_1 and T_2 values as well as standard deviations per vial at the iterations with lowest RMSRE values as well as the filtered versions of the final iterations are shown in Fig. 9. The T_1 values obtained from both the Cartesian and the radial reconstructions are in excellent

agreement with the reference values. For T_2 we observe good agreement but the deviations from the reference values are larger compared to T_1. This may be explained by potential errors in the B_1^+ maps used in the reconstructions that mostly have an impact on estimated T_2 values [37]. As observed before from Fig. 8, the vials with the highest T_2 values have not converged yet at the optimal iterations. The efficiencies per vial are displayed in 9c-d. At the optimal iterations, the radial case results in higher efficiencies in all vials(except for T_1 in vial number ten). However, at the (filtered) final iterations, a significant drop in efficiencies is observed for the radial case and the Cartesian case results in higher
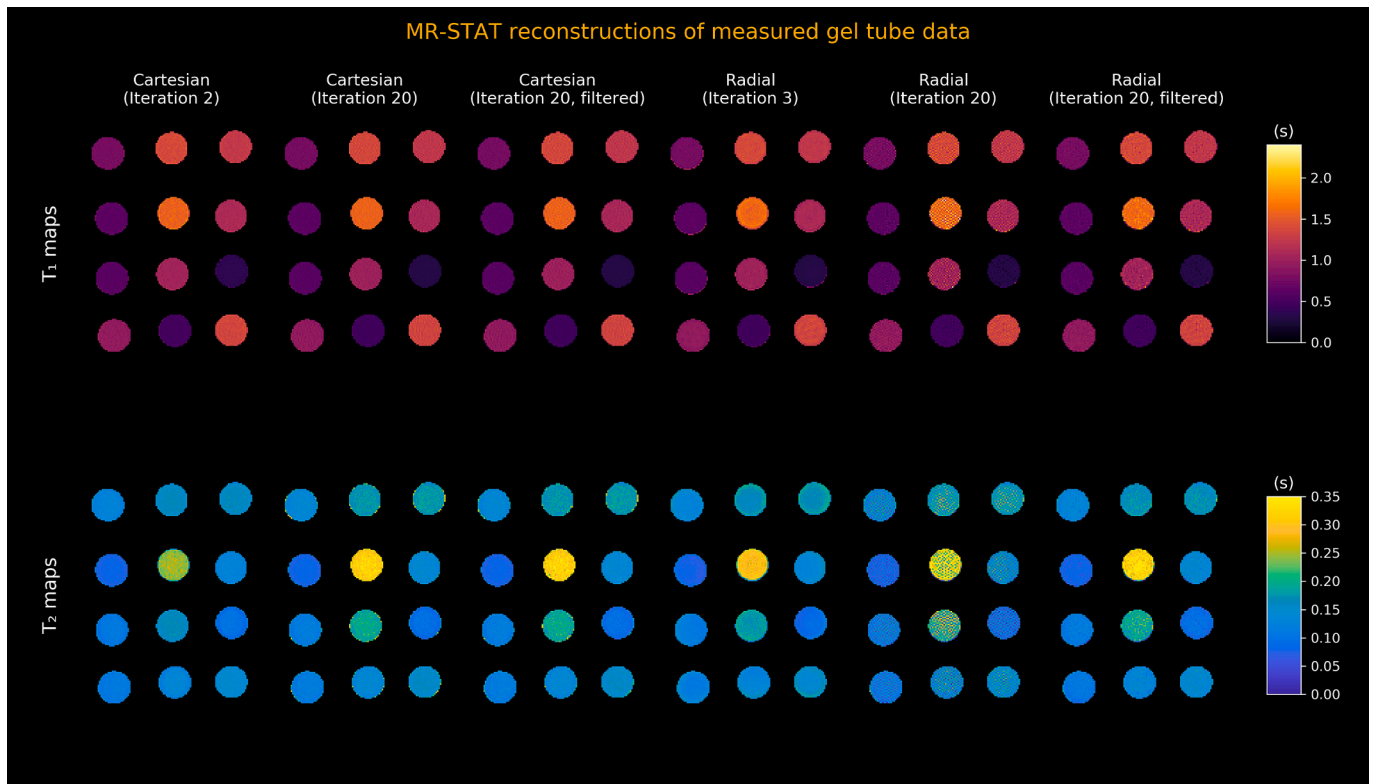
Fig. 8. The T_1 and T_2 parameter maps reconstructed from measured gel phantom data. The first two columns show the Cartesian reconstructions at the optimal iteration (two) and the final iteration (twenty). In columns four and five the corresponding radial reconstructions are shown. It can be observed that - unlike in the simulation study - the radial reconstruction is highly susceptible to overfitting artefacts and applying a filter is deemed necessary. The filtered maps are shown in columns three (Cartesian) and six (radial). For the Cartesian case, the effect of the filter is difficult to observe visually. For the radial case, it significantly reduces the high-frequency noise in the parameter maps.
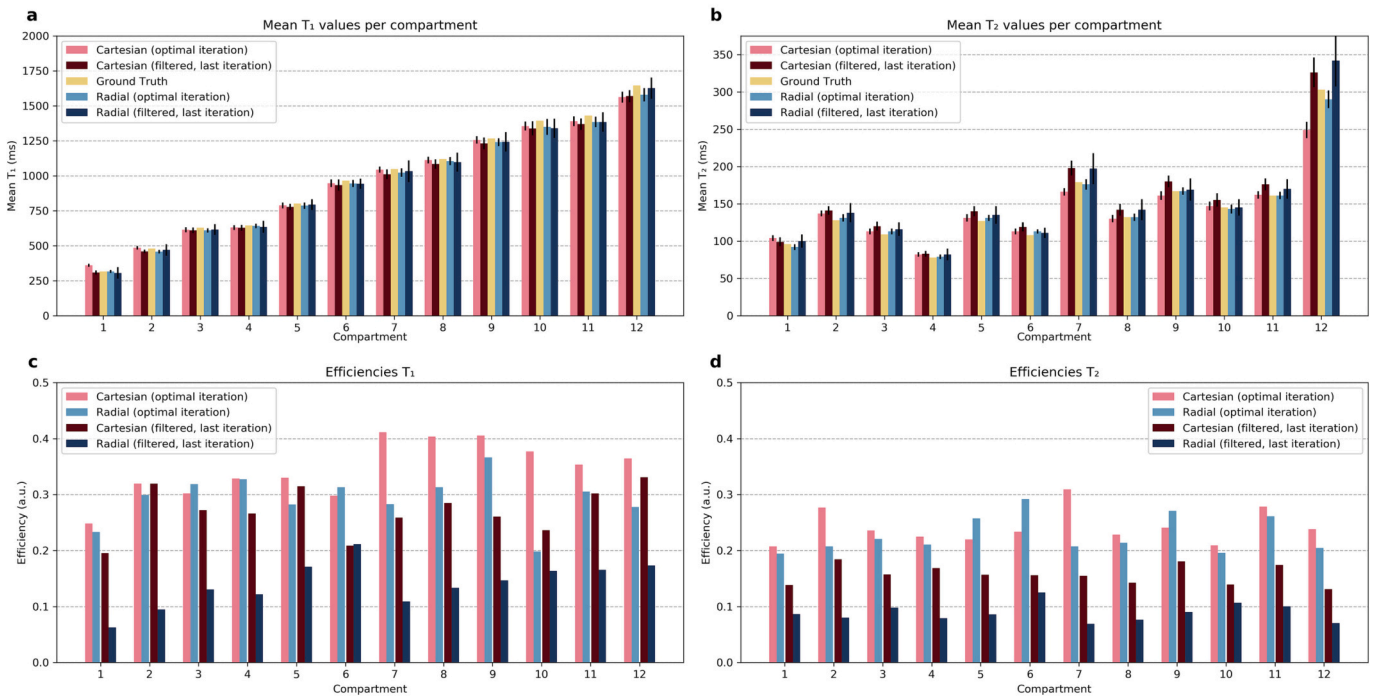
Fig. 9. Reconstruction results for the gel phantom measurements. **a-b**: Mean T_1 and T_2 values as well as standard deviations per vial of the gel phantom for the outer iterations with the lowest RMRSE values (two for Cartesian, three for radial) and the final iterations. **c-d**: Efficiencies per vial are shown. It can be observed that overall the radial case results in higher efficiencies at the optimal iterations while Cartesian case results in higher efficiencies at the latest iteration.

efficiencies in all vials (except for T_1 in vial number six).

3.3. In-vivo measurements

With no ground truth measurements available, the RMSRE values cannot be computed and an optimal iteration cannot be selected. Therefore we only consider the final iterations (i.e. iteration twenty) for both the Cartesian and radial cases. In Fig. 10, the T_1 and T_2 maps at these final iterations are shown. Like in the case for the gel phantoms, the radial reconstruction suffers from high frequency noise and windowing is deemed necessary. For this dataset, a Hann filter was utilized and the filtered maps are shown in Fig. 10 as well. Although the filtering greatly improves the quality of the radial parameter maps, some high frequency noise is still present after filtering (mostly in or around cerebrospinal fluid ("CSF") regions) whereas no high-frequency artefacts are observed to be present in the filtered Cartesian maps.

In the Cartesian reconstruction, the CSF appears to suffer from flow-induced artefacts that are known to be present in gradient-spoiled sequences as used in this work [38]. For the radial case these artefacts are much less severe, likely because the radial sampling pattern effectively results in the flow effects being averaged out over the whole duration of the acquisition.

Mean T_1 and T_2 values in gray- and white matter for the filtered maps as well as standard deviations and efficiencies are displayed in Table 1. Recent literature values [39] are also reported. For T_1, the Cartesian and radial reconstructions result in similar mean values in gray- and white matter and these values are in line with literature values. For T_2 the mean values for white matter between Cartesian and radial agree but in gray matter there is a larger discrepancy between the Cartesian and radial cases. Segmenting the gray matter is more challenging and segmentation errors may partly explain the larger discrepancy and larger standard deviations.

In terms of efficiency, the radial reconstruction results in higher efficiencies in white matter (0.098 vs 0.144 for T_1, 0.055 vs 0.065 for T_2)

whereas for gray matter the efficiencies are similar to their Cartesian counterparts (0.091 vs 0.088 for T_1, 0.033 vs 0.03 for T_2).

4. Discussion

In this work we have extended the MR-STAT framework with non-Cartesian gradient trajectories with the main purpose of comparing Cartesian and radial MR-STAT in terms of robustness and time-efficiency. Because MR-STAT uses a model-based iterative reconstruction in which spatial and dynamic encoding are coupled, providing predictions upfront on which acquisition type will result higher efficiencies is challenging. We therefore performed an empirical study based on simulations and experiments instead.

In general, errors in the reconstructed parameter maps (which directly influence the efficiency) are the result of thermal noise on the measured data, undersampling and/or imperfections in the signal model used in the reconstruction (due to e.g. hardware imperfections). The parameter maps reconstructed from the Cartesian noiseless numerical brain phantom dataset did not suffer from any undersampling (i.e. aliasing) artefacts despite the high undersampling factor used (one readout per contrast). Also in the radial case no streaking artefacts were observed in the reconstructed maps. Both Cartesian and radial MR-STAT are therefore robust against undersampling. However, in the radial case the outer k-space corners were never sampled and therefore the smaller, more narrow structures and tissue boundaries could not be properly resolved. As such, radial MR-STAT has a lower spatial encoding efficiency compared to Cartesian MR-STAT. For the numerical brain phantom datasets corrupted with simulated thermal noise, we observed that the radial reconstruction resulteded in higher T_2 time-efficiencies (by approximately 25%) compared to the Cartesian reconstruction in most tissue types. We hypothesize these higher efficiencies result from the fact that with the radial acquisition the center of k-space is sampled with each readout, and as such it has higher dynamic encoding power which compensates for the reduced spatial encoding that was observed
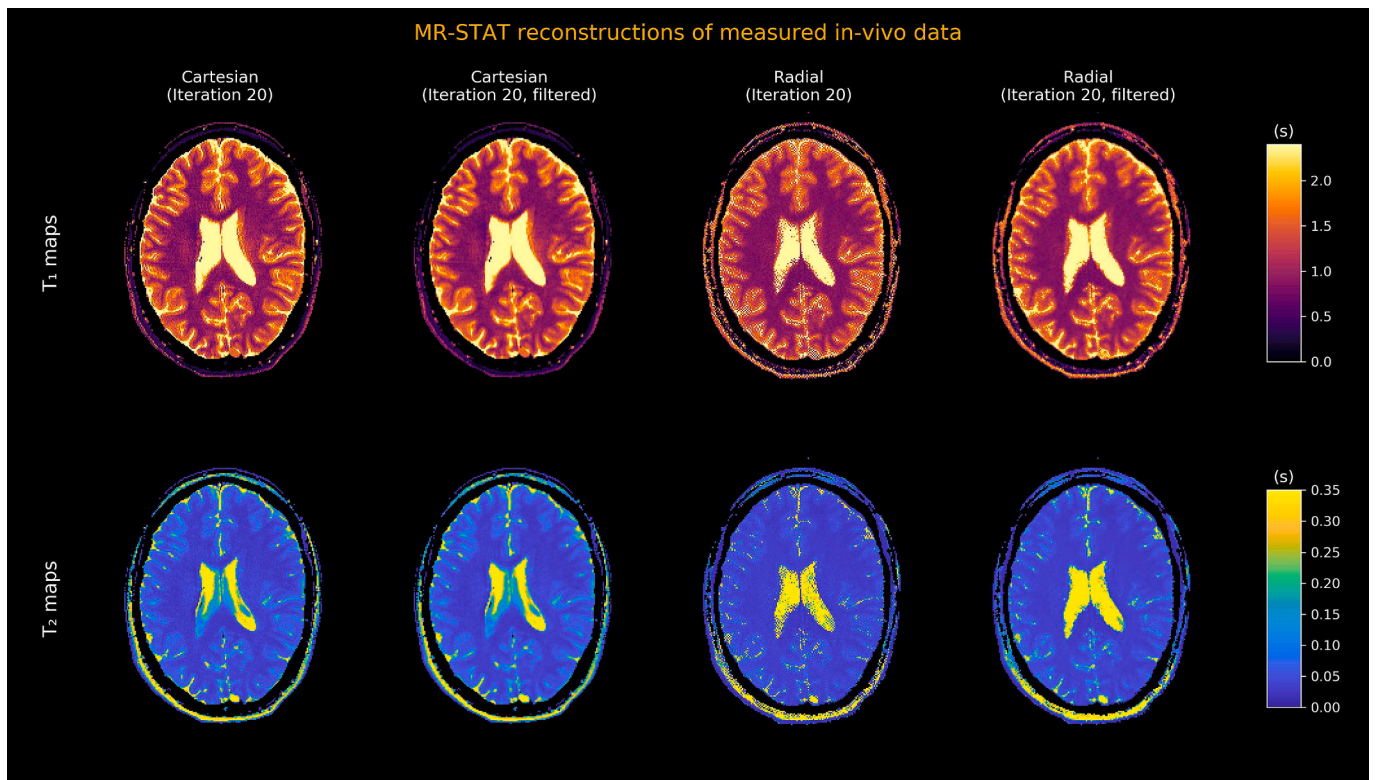

Fig. 10. Reconstruction results for the in vivo measurements. The Cartesian reconstructions at their final iterations are shown in the first (unfiltered) and second (Hann-filtered) columns. The radial reconstructions at their final iterations are shown in the third (unfiltered) and fourth (Hann-filtered) columns.

Table 1

Mean values, standard deviations and efficiencies for in vivo T_1 and T_2 in gray- and white matter regions. Literate values [39] are reported in the last column.

		Cartesian		Radial		Literature
		Mean ± Std (ms)	Efficiency (a.u.)	Mean ± Std (ms)	Efficiency (a.u.)	Mean (ms)
White Matter	T1	898.4 ± 78.0	0.098	881.3 ± 49.3	0.144	954
	T2	32.2 ± 5.0	0.055	31.4 ± 3.9	0.065	38.7
Gray Matter	T1	1471.4 ± 137.7	0.091	1398.1 ± 128.8	0.088	1372
	T2	57.7 ± 14.7	0.033	45.3 ± 12.2	0.03	52.7

in the noiseless numerical phantom reconstruction. For T_1 the radial reconstruction only results in higher efficiencies in gray- and white matter (and only slightly in skin). The difference between T_1 and T_2 may be explained by the presence of the inversion prepulse. This prepulse adds strong dynamic T_1 encoding to both acquisitions to the point where the intrinsic higher dynamic encoding of the radial acquisition may provide little to no benefit. On the other hand, the reduced spatial encoding for radial is still present, resulting in lower efficiencies in finer structures for the radial acquisition.

In the gel phantom measurements, we observed that - while the Cartesian reconstruction procedure results in an RMSRE curve that is similar to the noisy brain simulation case - for the radial case the situation is different because the reconstruction procedure is highly susceptible to overfitting. In terms of sources of errors in the parameter maps, the main difference between the numerical simulation study and the gel phantom study is the presence of potential model inaccuracies in the latter. For radial (or more general: non-Cartesian) acquisitions it is known that they are more sensitive to hardware imperfections (e.g. gradient delays) as compared to Cartesian acquisitions [40]. We thus hypothesize that the differences between the simulation results and the gel phantom results come from inaccuracies in the forward model due to hardware imperfections and that these inaccuracies result in high-frequency artefacts in the parameter maps at the later iterations of the reconstruction procedure. In that scenario, the benefits of higher dynamic encoding for radial that was observed in the noisy numerical brain phantom case is overshadowed by the presence of these artefacts. We also observed that at the "optimal" iterations, the vials with the highest $T2$ had not yet fully converged. An early stopping strategy thus poses a risk of introducing a signficant bias in the parameter maps. As an alternative strategy to reduce the impact of the high-frequency artefacts on the radial reconstructions we applied a k-space filter to the parameter maps in a post-processing step (similar to Pruessmann et al. [35]). Even after the filtering step, the Cartesian acquisition remained more efficient.

In both the noisy numerical brain phantom and gel phantom experiments the cost and RMSRE values had stabilized at iteration twenty. We therefore assumed in this work that twenty iterations would be sufficient for convergence in the in vivo reconstructions as well. At these final iterations, the application of a (Hann) filter was again considered necessary for the radial reconstruction. For the filtered reconstructions, the radial case resulted in higher efficiencies in white matter and comparable efficiencies in gray matter. However, some of the high spatial-frequency artefacts remained visible in the radial parameter maps even after filtering, which may hamper the clinical acceptability. We expect the impact of these artefacts to be even stronger on older MR systems with less performant gradient systems and less advanced eddy-current compensation mechanisms. The necessity of the filtering also complicates the reconstruction procedure in the sense that it involves more tweaking parameters (e.g. filter type and strength). The Cartesian reconstruction, like in the simulations and gel phantom experiments, did not display severe high-frequency artefacts. Filtering was not considered necessary but could still be desirable for visualisation of the parameter maps.

Over the entire range of experiments performed in this work, Cartesian MR-STAT was able to produce tissue parameter maps without apparent aliasing or overfitting artefacts. The reconstruction procedure

was robust against the number of iterations in the reconstruction in all cases, displayed similar behaviour in both simulations and measurements and required less tweaking parameters compared to radial MR-STAT. The combination of these factors may make Cartesian MR-STAT preferable over radial MR-STAT in a clinical setting despite the lower efficiency in white matter.

An additional downside of the radial acquisitions that is not taken into account in the current analysis is the effects of off-resonances. Whereas with Cartesian acquisitions the presence of off-resonances causes shifts in the image, with radial acquisitions, because the readout direction is different each TR, off-resonances will have a blurring effect on the reconstructed images. It should be noted though that with MR-STAT the off-resonance effects during readouts can be included in the forward model. As such, it should be possible to correct for this blurring effect by providing a separately measured off-resonance map to the reconstruction algorithm. Alternatively, a sequence could be designed that allows for the joint estimation of off-resonance maps with the T_1, T_2 and proton-density maps [41].

In the current work, we did not use a density compensation function for the radial reconstruction to compensate for the fact that the lower spatial frequencies are over-represented. Using such a density compensation, for example the Ram-Lak filter, as a pre-conditioner may result in faster convergence. We expect the (unfiltered) final parameter maps to suffer from the the the same high-frequency errors as in the reconstructions without density compensation. Reducing the number of iterations may aid in lowering reconstruction times for radial MR-STAT.

Instead of applying post-processing k-space filters, a more principled approach to suppress high frequency artefacts during reconstructions would be to add a spatial regularization term to the parameter maps in the MR-STAT objective function. This would, however, add additional complexity into the reconstruction procedure (e.g. choice of regularization function(s) and parameter(s), potential non-differentiability of the regularization term). At the same time we expect the outcomes to be the same: for radial, regularization would be necessary to stabilize the reconstructions whereas for Cartesian it is not necessary (but it may still be used to reduce noise in the reconstructed parameter maps).

One important limitation of this work is that we only considered a single RF train type in all acquisitions. The RF train was designed such that its local maxima were incoherent with respect to the sampling of the k-space center for the Cartesian acquisitions [42]. No optimization schemes were applied. For the radial case, since all readouts cover equivalent portions of k-space, it may not be necessary to take the spatial encoding into account such that the optimization can focus purely on enhancing the dynamic encoding power [43,44]. In the Cartesian case however, different readouts cover distinct parts of k-space and the optimization will have to strike a balance between spatial and dynamic encoding power. Performing such an optimization is non-trivial and is outside the scope of this work [45]. Since optimization schemes for Cartesian and radial can result in different RF trains for both, the efficiencies and conclusion drawn in the current work may be influenced when considering such optimized sequences.

Another limitation of this work is that we only considered 2D acquisitions in this work. For 3D acquisitions, we expect an amplification of the the dynamic encoding benefits of radial over Cartesian. Hardware imperfections in radial acquisitions remain an issue also at 3D and future research will be aimed better understanding and mitigating the impact

of these imperfections on the radial reconstructions, for example by utilizing gradient impulse response functions [46] to correct the gradient trajectory in the forward model (Eq. (1)).

5. Conclusion

We extended the MR-STAT framework to non-Cartesian acquisitions and compared Cartesian and radial MR-STAT in terms of robustness and time-efficiency. While radial MR-STAT resulted in higher T_2 efficiencies in numerical simulations, in the gel phantom experiment the efficiencies were lower compared to Cartesian MR-STAT and we argue this is due to increased sensitivity to hardware imperfections. In clinical practice, the robustness and reliability of Cartesian MR-STAT may be preferred, especially on older MR systems where the impact of hardware imperfections on the radial reconstructions are expected to be more severe. With this work we thus would like emphasize that Cartesian acquisitions are still highly relevant in the field of multi-parametric qMRI.

CRediT authorship contribution statement

Oscar van der Heide: Conceptualization, Software, Validation, Formal-analysis, Writing-original-draft, Visualization. **Alessandro Sbrizzi:** Conceptualization, Resources, Supervision, Writing-review-editing, Funding-acquisition. **Cornelis A.T. van den Berg:** Supervision, Resources, Writing-review-editing, Funding-acquisition.

Acknowledgments

Appendix A. Supplementary data

Supplementary data associated with this article can be found, in the online version, at https://doi.org/10.1016/j.mri.2023.01.017.

References

[1] Gernot Bielke M, Meves S Meindl, Brückner A, Rinck P, von Seelen W, Pfannenstiel P. A systematic approach to optimization of pulse sequences in NMR-imaging by computer simulations. In: Technology of Nuclear Magnetic Resonance. The Society of Nuclear Medicine; 1984.

[2] Bobman Stuart A, Riederer Stephen J, Lee James N, Suddarth Steven A, Wang Henry Z, Drayer Burton P, MacFall James R. Cerebral magnetic resonance image synthesis. Am. J. Neuroradiol. 1985;6(2):265–9.

[3] Deoni Sean CL. Quantitative relaxometry of the brain. Top. Magn. Reson. Imaging 2010.

[4] Tofts Paul. Quantitative MRI of the Brain. Chichester, UK: John Wiley & Sons Ltd.; Aug 2003.

[5] Ma Dan, Gulani Vikas, Seiberlich Nicole, Liu Kecheng, Sunshine Jeffrey L, Duerk Jeffrey L, Griswold Mark A. Magnetic Resonance Fingerprinting. Nature 2013;495:187–92.

[6] Gómez Pedro A, Cencini Matteo, Golbabaee Mohammad, Schulte Rolf F, Pirkl Carolin, Horvath Izabela, Fallo Giada, Peretti Luca, Tosetti Michela, Menze Bjoern H, et al. Rapid three-dimensional multiparametric MRI with quantitative transient-state imaging. Sci. Rep. 2020;10(1):1–17.

[7] Wang Fuyixue, Dong Zijing, Reese Timothy G, Rosen Bruce, Wald Lawrence L, Setsompop Kawin. 3D Echo Planar Time-resolved Imaging (3D-EPTI) for ultrafast multi-parametric quantitative MRI. NeuroImage 2022;250:118963.

[8] Stolk Christiaan C, Sbrizzi Alessandro. Understanding the Combined Effect of k-Space Undersampling and Transient States Excitation in MR Fingerprinting Reconstructions. IEEE Trans. Med. Imaging 2019;38(10):2445–55.

[9] Jiang Yun, Ma Dan, Seiberlich Nicole, Gulani Vikas, Griswold Mark A. MR fingerprinting using fast imaging with steady state precession (FISP) with spiral readout. Magn. Reson. Med. 2015;74(6):1621–31.

[10] Assländer Jakob, Glaser Steffen J, Hennig Jürgen. Pseudo Steady-State Free Precession for MR-Fingerprinting. Magn. Reson. Med. Mar 2017;77(3):1151–61.

[11] Cruz Gastao, Schneider Torben, Bruijnen Tom, Gaspar Andreia S, Botnar René M, Prieto Claudia. Accelerated Magnetic Resonance Fingerprinting using soft-weighted key-hole (MRF-SOHO). PloS One 2018;13(8):e0201808.

[12] Cloos Martijn A, Knoll Florian, Zhao Tiejun, Block Kai T, Bruno Mary, Wiggins Graham C, Sodickson Daniel K. Multiparametric imaging with heterogeneous radiofrequency fields. Nat. Commun. 2016;7(1):1–10.

[13] Buonincontri Guido, Sawiak Stephen J. MR fingerprinting with simultaneous B1 estimation. Magn. Reson. Med. 2016;76(4):1127–35.

[14] Doneva Mariya, Amthor Thomas, Koken Peter, Sommer Karsten, Börnert Peter. Matrix completion-based reconstruction for undersampled magnetic resonance fingerprinting data. Magn. Reson. Imaging 2017.

[15] Koolstra Kirsten, Beenakker Jan-Willem Maria, Koken Peter, Webb Andrew, Börnert Peter. Cartesian MR fingerprinting in the eye at 7T using compressed sensing and matrix completion-based reconstructions. Magn. Reson. Med. 2019;81 (4):2551–65.

[16] Block Kai Tobias, Uecker Martin, Frahm Jens. Model-based iterative reconstruction for radial fast spin-echo MRI. IEEE Trans. Med. Imaging 2009;28(11):1759–69.

[17] Sumpf Tilman J, Uecker Martin, Boretius Susann, Frahm Jens. Model-based nonlinear inverse reconstruction for T2 mapping using highly undersampled spin-echo MRI. J. Magn. Reson. Imaging 2011;34(2):420–8.

[18] Knoll Florian, Raya José G, Halloran Rafael O, Baete Steven, Sigmund Eric, Bammer Roland, Block Tobias, Otazo Ricardo, Sodickson Daniel K. A model-based reconstruction for undersampled radial spin-echo DTI with variational penalties on the diffusion tensor. NMR Biomed. 2015;28(3):353–66.

[19] Wang Xiaoqing, Roeloffs Volkert, Klosowski Jakob, Tan Zhengguo, Voit Dirk, Uecker Martin, Frahm Jens. Model-based T1 mapping with sparsity constraints using single-shot inversion-recovery radial FLASH. Magn. Reson. Med. 2018;79(2): 730–40.

[20] Zhao Bo, Lu Wenmiao, Kevin Hitchens T, Lam Fan, Ho Chien, Liang Zhi-Pei. Accelerated MR parameter mapping with low-rank and sparsity constraints. Magn. Reson. Med. 2015;74(2):489–98.

[21] Sbrizzi Alessandro, Heide Oscar van der, Cloos Martijn, Toorn Annette van der, Hoogduin Hans, Luijten Peter R, van den Berg Cornelis AT. Fast quantitative MRI as a nonlinear tomography problem. Magn. Reson. Imaging 2018;46:56–63.

[22] Heide Oscar van der, Sbrizzi Alessandro, Luijten Peter R, van den Berg Cornelis AT. High resolution in-vivo MR-STAT using a matrix-free and parallelized reconstruction algorithm. NMR Biomed. 2020;33(4):e4251.

[23] Hanna Liu, Oscar van der Heide, Cornelis A.T. van den Berg, Alessandro Sbrizzi, Accelerated MR-STAT Algorithm: Achieving 10-minute High-Resolution Reconstructions on a Desktop PC, in: Proc. Intl. Soc. Mag. Reson. Med., 2020.

[24] van der Heide Oscar, Sbrizzi Alessandro, van den Berg Cornelis AT. Accelerated MR-STAT reconstructions using sparse Hessian approximations. IEEE Trans. Med. Imaging 2020.

[25] Crawley Adrian P, Henkelman R Mark. A comparison of one-shot and recovery methods in T1 imaging. Magn. Reson. Med. 1988;7(1):23–34.

[26] Tsai Chi-Ming, Nishimura Dwight G. Reduced aliasing artifacts using variable-density k-space sampling trajectories. Magn. Reson. Med.: Offic. J. Int. Soc. Magn. Reson. Med. 2000;43(3):452–8.

[27] Aubert-Broche Berengere, Evans Alan C, Collins Louis. A new improved version of the realistic digital brain phantom. NeuroImage Aug 2006;32(1):138–45.

[28] Brown Robert W, Norman Cheng Y-C, Mark Haacke E, Thompson Michael R, Venkatesan Ramesh. Magnetic resonance imaging: physical principles and sequence design. John Wiley & Sons; 2014.

[29] Weigel Matthias. Extended phase graphs: dephasing, RF pulses, and echoes-pure and simple. J. Magn. Reson. Imaging 2015;41(2):266–95.

[30] Golub Gene H, Pereyra Victor. The differentiation of pseudo-inverses and nonlinear least squares problems whose variables separate. SIAM J. Numer. Anal. 1973;10 (2):413–32.

[31] Paige C, Saunders M. An algorithm for sparse linear equations and sparse least squares. ACM Trans. Math. Softw. 1982.

[32] Buehrer Martin, Pruessmann Klaas P, Boesiger Peter, Kozerke Sebastian. Array compression for MRI with large coil arrays. Magn. Reson. Med. 2007.

[33] Uecker Martin, Lai Peng, Murphy Mark J, Virtue Patrick, Elad Michael, Pauly John M, Vasanawala Shreyas S, Lustig Michael. ESPIRiT-an eigenvalue approach to autocalibrating parallel MRI: Where SENSE meets GRAPPA. Magn. Reson. Med. Mar 2014;71(3):990–1001.

[34] Stollberger Rudolf, Wach Paul. Imaging of the active B1 field in vivo. Magn. Reson. Med. 1996;35(2):246–51.

[35] Pruessmann Klaas P, Weiger Markus, Börnert Peter, Boesiger Peter. Advances in sensitivity encoding with arbitrary k-space trajectories. Magn. Reson. Med.: Offic. J. Int. Soc. Magn. Reson. Med. 2001;46(4):638–51.

[36] Zhang Yongyue, Brady Michael, Smith Stephen. Segmentation of brain MR images through a hidden Markov random field model and the expectation-maximization algorithm. IEEE Trans. Med. Imaging 2001;20(1):45–57.

[37] Olsson Hampus, Andersen Mads, Helms Gunther. Reducing bias in DREAM flip angle mapping in human brain at 7T by multiple preparation flip angles. Magn. Reson. Imaging 2020;72:71–7.

[38] Lisanti Christopher, Carlin Carrie, Banks Kevin P, Wang David. Normal MRI appearance and motion-related phenomena of CSF. Am. J. Roentgenol. 2007;188 (3):716–25.

[39] Körzdörfer Gregor, Kirsch Rainer, Liu Kecheng, Pfeuffer Josef, Hensel Bernhard, Jiang Yun, Ma Dan, Gratz Marcel, Bär Peter, Bogner Wolfgang, et al. Reproducibility and repeatability of MR fingerprinting relaxometry in the human brain. Radiology 2019;292(2):429–37.

[40] Smith Travis B. MRI artifacts and correction strategies. Imag. Med. 2010;2(4):445.

[41] Körzdörfer Gregor, Jiang Yun, Speier Peter, Pang Jianing, Ma Dan, Pfeuffer Josef, Hensel Bernhard, Gulani Vikas, Griswold Mark, Nittka Mathias. Magnetic resonance field fingerprinting. Magn. Reson. Med. 2019;81(4):2347–59.

[42] Miha Fuderer, Oscar van der Heide, Hongyan Liu, Cornelis A.T. van den Berg, Alessandro Sbrizzi, Non-steady-state sequences for multi-parametric MRI need to be evaluated in the context of gradient-encoding, in: Proc. Intl. Soc. Mag. Reson. Med., 2022.

[43] Assländer Jakob, Lattanzi Riccardo, Sodickson Daniel K, Cloos Martijn A. Optimized quantification of spin relaxation times in the hybrid state. Magn. Reson. Med. 2019.

[44] Alessandro Sbrizzi, Tom Bruijnen, Oscar van der Heide, Peter Luijten, Cornelis A.T. van den Berg, Dictionary-free MR Fingerprinting reconstruction of balanced-GRE sequences, Nov 2017.

[45] Miha Fuderer, Efficient performance analysis and optimization of transient-state sequences for multi-parametric MRI, 4 2022.

[46] Vannesjo Signe J, Haeberlin Maximilan, Kasper Lars, Pavan Matteo, Wilm Bertram J, Barmet Christoph, Pruessmann Klaas P. Gradient system characterization by impulse response measurements with a dynamic field camera. Magn. Reson. Med. 2013;69(2):583–93.